PNAS RESEARCH ARTICLE | BIOCHEMISTRY

Mass spectrometry footprinting reveals how kinetic stabilizers counteract transthyretin dynamics altered by pathogenic mutations

Francisca Pinheiro[a,1,2], Ravi Kant[b,1,3], Saketh Chemuru[b], Nathalia Varejão[a], Adrián Velázquez-Campoy[c,d,e,f], David Reverter[a], Irantzu Pallarès[a,4], Michael L. Gross[b,4], and Salvador Ventura[a,g,4]

Affiliations are included on p. 10.

Edited by Jeffery Kelly, Scripps Research, La Jolla, CA; received July 25, 2025; accepted November 19, 2025

The aggregation of transthyretin (TTR) results in life-threatening transthyretin amyloidosis. Familial forms of the disease arise from point mutations that destabilize the TTR tetramer, leading to its dissociation and/or monomer unfolding and subsequent formation of amyloid fibrils. Small molecules that kinetically stabilize the native tetramer effectively inhibit this aggregation. Although over 300 X-ray crystal structures of TTR have been determined, these data refer to a static structure and do not capture the conformational effects of mutations and ligand binding. Here, we demonstrate that hydrogen–deuterium exchange (HDX) and fast photochemical oxidation of proteins (FPOP) coupled with mass spectrometry (MS) offer critical insights into the conformational dynamics associated with TTR amyloidogenic mutations and the binding of kinetic stabilizers. The results indicate that the design of TTR binders should consider the specific conformational traits of each TTR pathogenic variant. We propose that incorporating MS-based techniques into TTR drug discovery will expedite the development of effective pathology-specific aggregation inhibitors.

protein dynamics | fast photochemical oxidation of proteins (FPOP) | hydrogen/deuterium exchange mass spectrometry (HDX-MS) | transthyretin

Significance

Transthyretin (TTR) misfolding and aggregation underlie a group of fatal diseases known as TTR amyloidosis. Pathogenic mutations decrease the protein's stability, enhancing TTR amyloidogenicity. While TTR-stabilizing molecules prevent aggregation, currently approved drugs do not fully address the diverse disease phenotypic spectrum, underscoring the need for new stabilizers. High-resolution structures of TTR and TTR/inhibitor complexes have guided therapeutic design for decades. Yet, these structures are almost superimposable and fail to capture the dynamic effects of mutations and of ligand binding. Here, we show that HDX-MS and FPOP-MS reveal key conformational changes and long-range interactions that are invisible to crystallography. These insights reveal previously hidden mechanisms of TTR destabilization and lay the groundwork for designing mutation-specific kinetic stabilizers with enhanced therapeutic potential.

Misfolding of human transthyretin (TTR) results in the accumulation of amyloid fibrils in various tissues, leading to distinct progressive clinical syndromes known as transthyretin amyloidosis (ATTR) (1).

TTR is a homotetramer consisting of four subunits of 127 amino acids each, termed A, B, C, and D. Each subunit folds as a β-sandwich, with two β-sheets comprising the DAGH strands and CBEF strands, and with a short helix at the C-terminal end of the E strand. The monomers associate via their edge β-strands to form two dimers (AB and CD) that further associate back-to-back in the tetramer. The AB/CD dimer–dimer interface defines two identical thyroxine (T_4)-binding sites at opposite sides of the molecule (*SI Appendix*, Fig. S1) (2, 3). TTR dissociation at the T_4-binding interface generates dimers that rapidly dissociate into amyloidogenic monomers (4, 5).

Pathogenic mutations in the TTR gene decrease tetramer and/or monomer stability, enhancing TTR amyloidogenicity (6, 7). Most disease-associated variants are linked to familial amyloid polyneuropathy (FAP) or cardiomyopathy (FAC) (8–10). Certain TTR mutations can also affect the central nervous system, giving rise to a rare form of ATTR known as leptomeningeal amyloidosis (11, 12). Of note, even wild-type TTR (WT-TTR) can aggregate with age, causing senile systemic amyloidosis, primarily manifesting as cardiomyopathy (13). Although numerous crystal structures of WT-TTR and pathogenic mutants have been determined, they have failed to reveal the structural basis that accounts for mutation-induced destabilization because the X-ray structures are virtually identical (7, 14).

Occupancy of the T_4-binding sites by small molecules stabilizes TTR tetramers, inhibiting dissociation and, thus, preventing the onset of ATTR (15). The most common TTR stabilizers in clinical practice are diflunisal, tafamidis, and acoramidis. Diflunisal, an FDA-approved nonsteroidal anti-inflammatory drug, is employed off-label for ATTR treatment, but its use can cause adverse effects related to its anti-inflammatory activity (16). Tafamidis is approved for the treatment of early-stage FAP in several countries, but not by the FDA (17). Recently, tafamidis was approved by the FDA for ATTR-related cardiomyopathy, both hereditary and wild-type forms (18). Acoramidis (formerly AG10) was approved last year for the same indication (19). Importantly, up to 30% of patients do not respond to tafamidis treatment, particularly those with advanced disease (20).

This article is a PNAS Direct Submission.

[1]F.P. and R.K. contributed equally to this work.

[2]Present address: Department of Molecular Biology and Genetics, Aarhus University, Aarhus C 8000, Denmark.

[3]Present address: University School of Biotechnology, Guru Gobind Singh Indraprastha University, New Delhi 110078, India.

[4]To whom correspondence may be addressed. Email: Irantzu.Pallares@uab.es, mgross@wustl.edu, or salvador.ventura@uab.es.

This article contains supporting information online at https://www.pnas.org/lookup/suppl/doi:10.1073/pnas.2519908122/-/DCSupplemental.

Published December 31, 2025.

Moreover, evidence suggests that tafamidis and acoramidis exhibit low blood–brain barrier permeability (21, 22), rendering them suboptimal for the treatment of leptomeningeal amyloidosis. Collectively, this highlights the need to develop new TTR stabilizers to attain a broader therapeutic coverage. However, Apo-TTR and TTR/inhibitor X-ray structures are almost superimposable, obscuring the structural determinants critical for tetramer stabilization and ligand design (23). Therefore, alternative methods are needed to capture the impact of mutations and ligands on TTR stability and conformation.

Mass spectrometry (MS)-based footprinting methods have become powerful tools for assessing protein structure and dynamics, including hydrogen–deuterium exchange (HDX) and fast photochemical oxidation of proteins (FPOP) (24, 25). HDX relies on the exchange of backbone amide hydrogens with deuterium to assess changes in solvent accessibility and hydrogen bonding and can provide a temporally and spatially resolved picture of the exchangeable amide H network (26–28). In FPOP, a pulsed laser is used to trigger the homolysis of hydrogen peroxide in solution, generating two hydroxyl radicals that label solvent-exposed amino acid side chains. This last type of labeling occurs faster (microsecond time scale) than HDX, is irreversible, and readily provides some residue-specific information (25, 29). When coupled to MS, these methods offer insights into the conformational changes induced by ligand binding and mutations under close-to-native conditions in solution (30–32).

In this study, we employed HDX-MS and FPOP-MS to identify the structural variations underlying the increased amyloidogenicity of the two most common TTR pathogenic mutations, V30M and V122I. We also used these methods to investigate the conformational changes induced by the binding of M-23 (33) and tolcapone (34, 35), two potent TTR kinetic stabilizers developed in the Ventura laboratory (*SI Appendix*, Fig. S2). Consistent with previous observations, the X-ray structures we obtained for the four ligand-bound complexes are nearly identical and cannot explain the distinct stabilizing effects observed for each compound. Thus, our results demonstrate that these MS-based footprinting techniques can accurately monitor stabilizing/destabilizing effects on TTR structure, making them attractive tools for developing TTR binders with selective and optimized stabilization activity for specific TTR mutants.

Results

Conformational Dynamics of WT-, V30M-, and V122I-TTR Assessed By HDX-MS. TTR mutants can be classified into two groups: those that experience kinetic destabilization, where the tetramer breaks apart more rapidly, leading to an increased aggregation rate, and those that are thermodynamically destabilized, where the monomer, once dissociated, misfolds readily into the amyloidogenic intermediate. The V122I mutation is the most common amyloidogenic variant, primarily associated with FAC (36), and it leads to a kinetically destabilized tetramer that dissociates roughly at twice the rate of WT-TTR, whereas the tertiary (monomer) stability of V122I is similar to that of the WT protein (7). The V30M mutation is the most prevalent pathogenic variant linked to FAP (10). Unlike V122I, V30M remains kinetically stable but is thermodynamically destabilized. In other words, the quaternary (tetramer) stability of V30M resembles that of WT-TTR, whereas the stability of the monomer is lower (6, 7). Despite these differences, the crystal structures of both V30M- and V122I-TTR are nearly identical to that of WT-TTR (*SI Appendix*, Fig. S3), with backbone RMSD (for structured residues) relative to WT of 0.28 and 0.23 Å, respectively. Importantly, it has been proposed that the combined thermodynamic and kinetic stability of TTR variants can help to predict disease severity (7), underscoring the importance of understanding how pathogenic mutations perturb tetramer and/or monomer stability.

To assess the impact of V30M and V122I mutations on TTR's structural dynamics/flexibility, we conducted HDX-MS experiments. We compared the results obtained for the mutants to those obtained for WT-TTR under the same conditions (37 °C, pH 7.4). To ensure that the majority of peptides provided sufficient spatial resolution, we used double enzymatic digestion, Fungal XIII followed by pepsin on both wild-type and variants. This approach generated a total of 225, 238, and 240 unique peptides, with average lengths of 13.1, 12.8, and 12.8, for WT-, V30M-, and V122I-TTR, respectively (*SI Appendix*, Fig. S4).

HDX-MS of WT-TTR alone shows that the peptides representing the N-terminus and the far C-terminus underwent rapid HDX, whereas most of the peptides across the protein exchanged more slowly. This indicates that the N and far C termini are less ordered and/or more dynamic than the majority of the structure, and the remaining secondary structural elements are located in a stable H-bonding network and/or less dynamic regions. The HDX kinetic profiles of WT-TTR are consistent with the crystal structure, with the exception that the first ten N-terminal residues and the last two C-terminal residues are often not seen by X-ray crystallography (23), suggesting that the amide hydrogens in most structural elements are involved in stabilizing the monomer and dimer interfaces (*SI Appendix*, Fig. S5).

After assessing the WT-TTR, we used HDX-MS to investigate V30M/V122I under the same conditions. For a more convincing comparison, only the common peptides with higher signal-to-noise ratios were used, still providing 100% sequence coverage in all cases. HDX for each peptide corresponding to a TTR variant was quantified by calculating the difference in cumulative deuterium uptake between WT-TTR and the respective variant (V30M or V122I), as shown in Fig. 1 *A* and *B* and in *SI Appendix*, Tables S1 and S2. In the supplementary tables, the values are expressed as percentage changes, indicating relative protection (negative values) or deprotection (positive values). One can view that an increase in HDX (%) indicates destabilization of the variant, whereas a decrease is in accord with structural stabilization.

The V30M mutation is located on β-strand B (Fig. 1*C*), where its side chain is buried in the protomer's hydrophobic core. This mutation induces differences in HDX throughout the entire structure, indicating long-range effects propagating from the mutation site. Increased HDX occurs for peptides covering the regions V14 to N28, M30 to E54, A81 to H90, and V94 to A109, whereas decreased HDX pertains in regions I73 to Y78 and A109 to V121 (Fig. 1 *A* and *C* and *SI Appendix*, Table S1). Two of the destabilized secondary structure elements are β-strand B, where the mutation resides, and β-strand C, with which V30 packs, both located in the front CBEF β-sheet. This effect propagates to β-strands D and G, and to a lesser extent to β-strand A in the back DAGH β-sheet. Surprisingly, the helix and β-strand H become less dynamic or more buried in V30M, indicating a significant conformational rearrangement.

The monomer–monomer interface, involving β-strands F (excluding the C-terminal segment) and H, is stabilized by the V30M mutation, as indicated by the increased protection observed in the H strand. In contrast, in the AB/CD dimer–dimer interface, involving the β-strand A, the AB loop, and β-strand G, structural effects are evident. Nevertheless, consistent with the proposed destabilization mechanism for this variant, the primary impact of V30M arises from the altered packing and dynamics of the

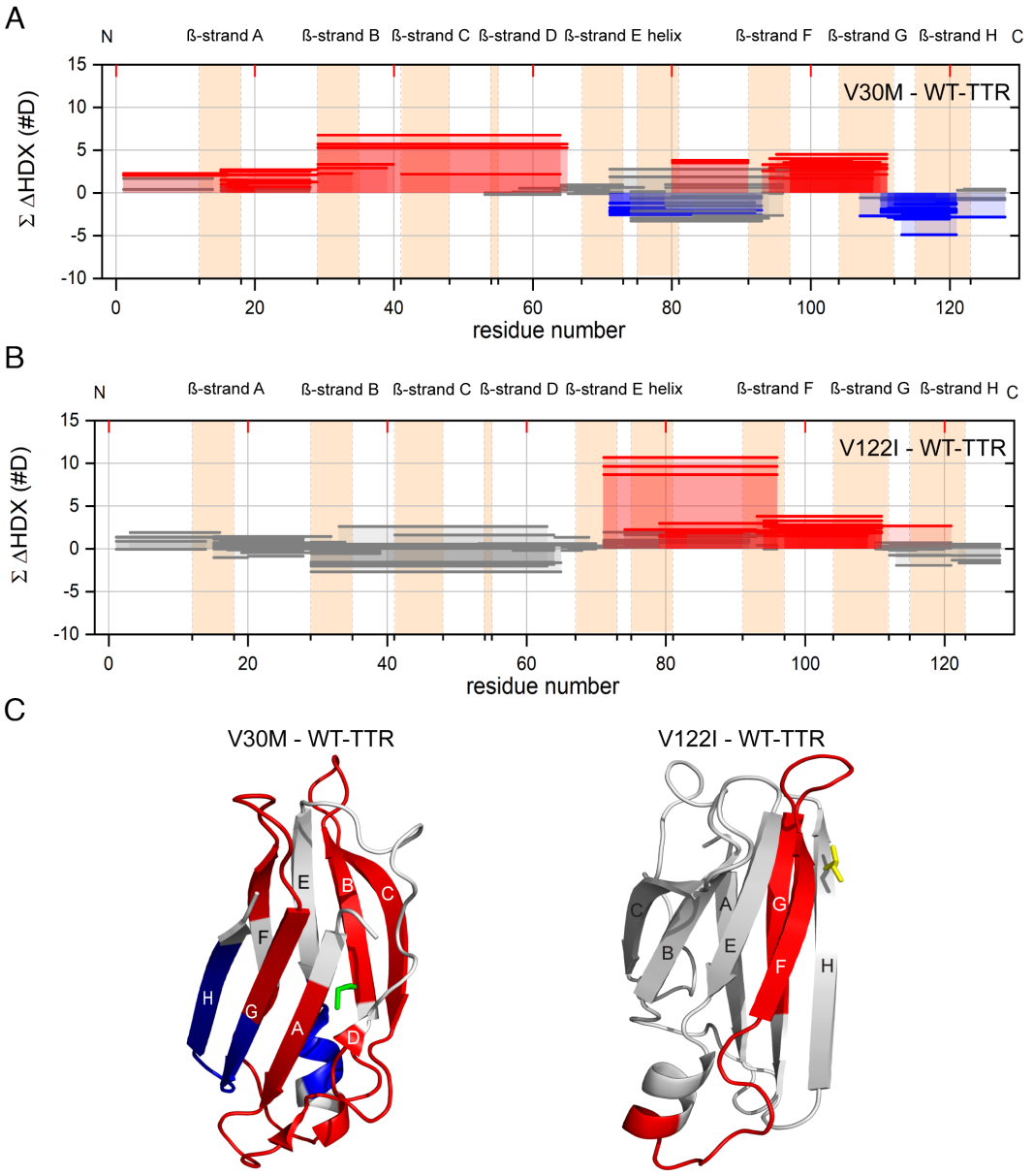

Fig. 1. Differences in backbone dynamics between WT-TTR and TTR variants V30M and V122I as assessed by HDX-MS. (*A* and *B*) The cumulative HDX differences of V30M minus those of WT-TTR (*A*) and of V122I minus WT-TTR (*B*) are shown in the Woods' plot format. Peptides are represented as horizontal lines; those that show statistically significant protection in blue, those with significant exposure in red, and those from regions that are unaffected in gray. Secondary structural elements of TTR are indicated on *Top* (peach shading). (*C*) Those regions that show statistically significant changes in HDX between WT-TTR and V30M-TTR (*Left*) or V122I-TTR (*Right*) are mapped onto the X-ray crystal structure of the proteins. Areas that are more exposed for the variants are in red, whereas those that are more protected are in blue. The side chains of M30 and I122 are shown as green and yellow sticks, respectively. Figure prepared from PDB structures 4TL4 (V30M-TTR) and 1TTR (V122I-TTR).

protomer itself, rather than the disruption of intersubunit contacts (6, 7).

The V122I mutation is located at the C-terminus of the H-strand (Fig. 1*C*), with its side chain projecting into a hydrophobic pocket formed by the side chains of Y105 and A120 on the same protomer, as well as F87 and Y114 on the neighboring subunit. The HDX kinetics of V122I-TTR are more similar to that of WT-TTR than to those of V30M-TTR (*SI Appendix*, Table S2). A significant increase in HDX, however, occurred for the peptides spanning K80 to A109, which includes part of the helix, β-strands F and G, and the connecting loops (Fig. 1 *B* and *D*).

This pattern indicates that structural perturbations propagate from the mutation site. The strong interface, involving β-strands F and H from neighboring subunits is stabilized by numerous hydrogen bonds and by the insertion of residue F87 (from strand F) into a hydrophobic pocket in the opposing subunit, packing against V122. The bulkier I122 side chain perturbs this packing, leading to increased HDX in strand F. This indicates that the mutation, although located within the weak dimer–dimer interface, indirectly affects the strong interface as well. Altogether, these data support the proposed mechanism for the V122I mutation: It primarily disrupts intersubunit interactions, promoting tetramer dissociation rather than intrinsic destabilization of the monomeric fold (6, 37).

M-23 and Tolcapone Binding to WT-TTR Promote Short- and Long-Distance Structural Stabilization As Revealed by HDX-MS and FPOP. After investigating the structural differences between TTR variants, we implemented HDX-MS to detect any effects of

tolcapone and M-23 on the TTR tetramer structure in solution. M-23 is a tolcapone derivative that binds WT-TTR with > 5-fold affinity than the parental molecule tolcapone, resulting in a higher tetramer stabilization both in vitro and in human plasma (33). Despite this, the X-ray structures of WT-TTR in complex with M-23 and tolcapone are almost completely superimposable (*SI Appendix*, Fig. S6).

HDX. We performed HDX-MS, as described above, except that, for the bound state, WT-TTR was incubated with the compounds for 2 h before being diluted in D_2O buffer. HDX for each peptide was quantified by a relative comparison of cumulative deuterium uptake between the unbound and ligand-bound WT (Fig. 2*A*). Relative changes (%) in deuterium uptake between the apo and ligand-bound form of WT-TTR are shown in *SI Appendix*, Table S3. As before, negative values (decreases in HDX) indicate structural protection, while positive values (increases in HDX) reflect structural destabilization (deprotection) and loosening of the structure.

Both compounds induced significantly decreased HDX for peptides spanning β-strand A and AB loop (V15-D19 and V17-N28), the EF-helix (K71-Y79), and β-strand G to H (A112-V121), reflecting decreased protein dynamics upon binding and/or structural compaction. These regions include residues known to interact with M-23 (33) and tolcapone (34) (e.g., K15 and T119), as well as residues distant from the binding pocket (Fig. 2*B* and *SI Appendix*, Fig. S7). Specifically, the loop between β-strands A and B (A19-V28) and part of the EF-helix (K70-Y78) become protected. The AB loop participates in the contacts that stabilize the weaker AB/CD dimer–dimer interface (2), whereas the EF-helix is involved in the interaction between subunits A(C) and B(D) in one dimer (38). Additionally, the EF-helix interacts with the AB loop; thus, changes in the EF-helix are likely to impact both TTR interfaces (38, 39).

The analysis of the kinetic curves of all WT-TTR peptides in the presence and absence of these stabilizers (*SI Appendix*, Fig. S5 and *SI Appendix*, Table S3) indicates that HDX differences are

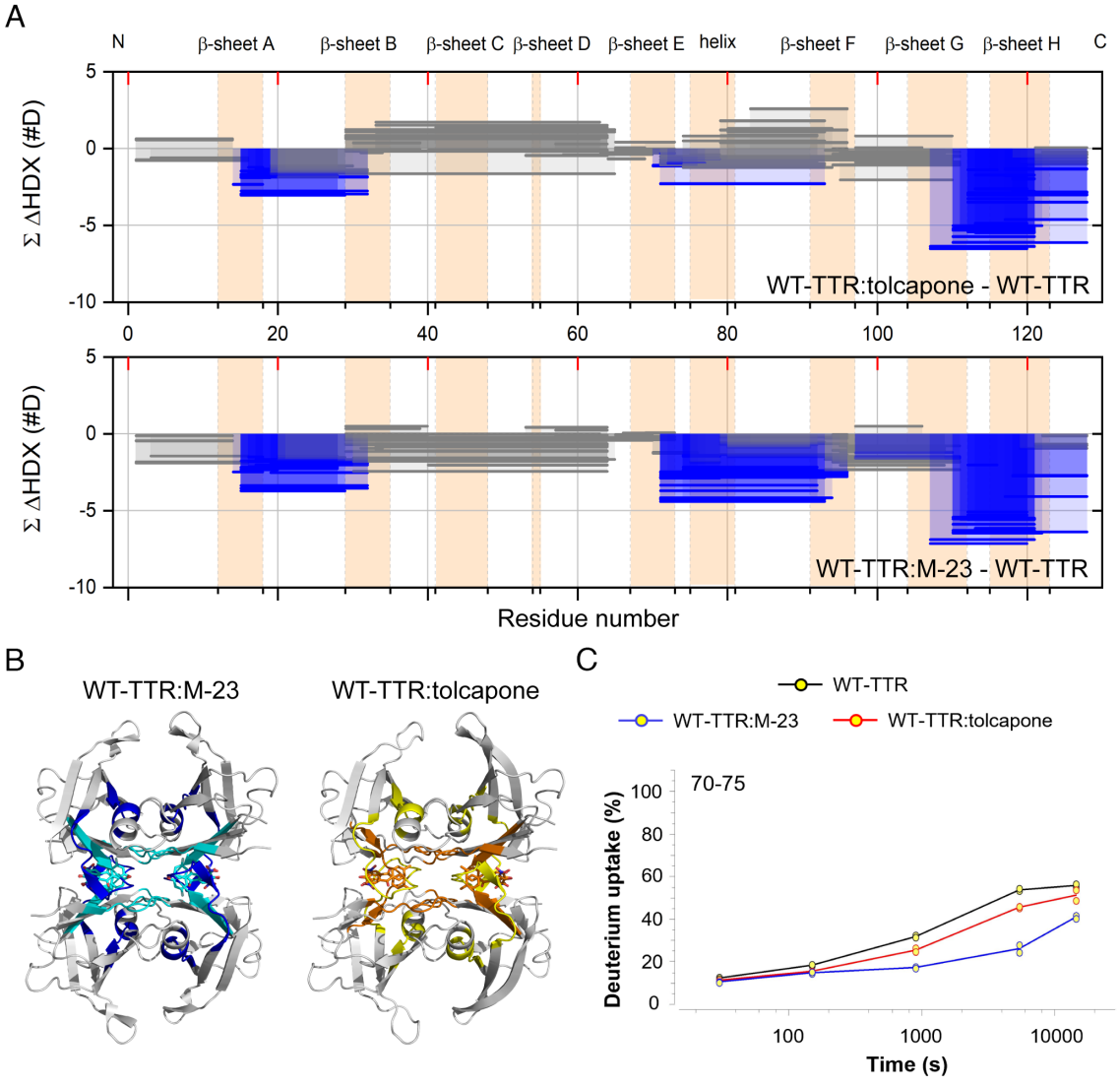

Fig. 2. Effect of M-23 and tolcapone on WT-TTR structure as examined by HDX-MS. (*A*) Woods' plots showing cumulative HDX differences (Y-axis) between the bound and unbound state for tolcapone (*Upper* panel) and M-23 (*Lower* panel). Secondary structure elements of TTR are designated on top of each panel (peach shading). Peptides with statistically significant protection are highlighted in blue, whereas those with significant exposure are in red. Peptides from unaffected areas are in gray. (*B*) Statistically significant changes in HDX are mapped onto the structure of the WT-TTR:M-23 complex (PDB: 7QC5) and the WT-TTR:tolcapone complex (PDB: 4D7B). The regions 19 to 28 (AB loop) and 70 to 78 (part of the EF-helix) are colored in either dark blue or yellow in the WT-TTR:M-23 and WT-TTR:tolcapone structures, respectively. Meanwhile, the regions closer to the binding pocket are shown in cyan in the WT-TTR:M23 structure and orange in the WT-TTR:tolcapone structure. (*C*) HDX kinetics of WT-TTR unbound (black) and bound to M-23 (blue) or tolcapone (red) for a peptide in the region of the EF-helix (residues 70 to 75).

more significant with M-23 than with tolcapone, especially in the β-strand A (11%) and EF-helix (12%) segments (Fig. 2*C*). This suggests that M-23 has a more pronounced stabilizing effect on WT-TTR than tolcapone, which is consistent with our previous findings (33).

FPOP. To identify the side chain interactions at the binding site of the small molecule on specific residues, FPOP experiments were conducted. Subsequently, changes in oxidation at those individual residue levels were analyzed by using MS/MS. Differences between the bound and unbound states showed that 16 residues were significantly protected from oxidation upon binding to M-23 and tolcapone. Interestingly, various residues from the N-terminus, middle, and C-terminus, displayed a decrease in oxidative modification when bound to the small molecules (Fig. 3*A*). To quantify the relative difference in oxidation, the percentage change measured in the presence of M-23 was compared with that for tolcapone. A negative difference (i.e., a decrease in percentage oxidation) indicates a greater protective effect of M-23 compared to tolcapone, whereas a positive difference (i.e., an increase in percentage oxidation) suggests that tolcapone provides superior protection over M-23 when bound to TTR (*SI Appendix*, Table S4).

We found distinct patterns for specific residues of WT-TTR for M-23 and tolcapone. Specifically, M-23 exhibited significantly lower oxidation levels in 11 out of 16 residues, indicating greater structural protection. In contrast, only two residues, S115/117 and Y114/116, showed a decrease in oxidative modification in the tolcapone-bound state compared to the M-23-bound state of WT-TTR (Fig. 3*A* and *SI Appendix*, Table S4). Residues V20 and T118 showed nearly equivalent oxidation between both compounds. Overall, these results suggest that M-23 confers broader and more substantial stabilization of the WT protein than tolcapone.

Not surprisingly, 9 out of the 16 identified residues are inside or near the binding pocket (M13, V14, V20, S50, E54, I84, Y114/116, S115/117, T118), indicating short-range alterations on side chain dynamics. These residues include E54 and S117, which are two of the key interacting residues identified in X-ray crystal structures of TTR:inhibitor complexes (33, 40, 41). Noteworthy, the remaining residues (P11, F33, E42, E51, T59/60, I68, Y69, D99/S100) are distant from the interaction site, revealing long-range conformational changes on the protein upon tolcapone and M-23 binding. On average, for both small molecules, the protective effect was more pronounced at residues V14 (β-strand A), V20 (AB loop), I68 (β-strand E), and S115/117, Y114/116, T118 (all in β-strand H) (Fig. 3*A*). These residues map within (V17-N28, A112-V121) or adjoin (V15-D19, K71-Y79) of the HDX-protected regions. Consistent with the HDX-MS data, M-23 binding had a more substantial protective effect than that of tolcapone, particularly on residues P11, I84, and D99/S100 (*SI Appendix*, Table S4). I84 in the EF loop is close to the binding site, whereas P11, at the N-terminal end of β-strand A and D99/S100 in the FG loop, are distant, indicating a potent long-range stabilizing effect for M-23 on WT-TTR (Fig. 3*B*).

M-23 and Tolcapone Reduce V30M- and V122I-TTR Conformational Flexibility. After demonstrating that HDX-MS and FPOP-MS can effectively monitor the impact of small-molecule stabilizers on protein structural dynamics of WT-TTR, we applied these approaches to analyze their effects on the TTR pathogenic variants V30M and V122I.

HDX. HDX-MS experiments (Fig. 4 *A* and *B*, *SI Appendix*, Tables S5 and S6) show that the overall effects of M-23 and tolcapone on V122I-TTR are similar (Fig. 4*B* and *SI Appendix*, Figs. S8 andS9), with regions 15 to 28 (β-strand A and AB loop), 70 to 78 (EF-helix), 95 to 109 (β-strand F to G), and 111 to 120 (β-strands G to H) undergoing less deuterium exchange after binding to the kinetic stabilizers, which again implies the occurrence of both short- and long-range conformational changes on the proteins upon interacting with these molecules (Fig. 4*C* and *SI Appendix*, Table S6). Roughly the same regions become protected in V30M-TTR (Fig. 4 *A* and *C* and *SI Appendix*, Fig. S9); however, the analysis of the kinetic curves of all V30M-TTR peptides in the presence and absence of the stabilizers (*SI Appendix*, Fig. S10) indicates that tolcapone confers 27% greater protection than M-23 in the C-terminal region of this protein (Fig. 4*D* and *SI Appendix*, Table S5). This region encompasses residues within the ligand-binding site, suggesting that, unexpectedly, tolcapone binds more strongly to the V30M variant than M-23.

To understand whether M-23 and tolcapone decrease the conformational flexibility of V30M and V122I variants to an extent that it approaches that of the WT protein in the absence of compounds (WT-Apo), we compared the HDX profiles for the different states (*SI Appendix*, Tables S7 and S8). The comparison between the WT-Apo and the ligand-bound states of M-23 and tolcapone with V122I and V30M variants revealed HDX protection at both the N and C termini, as well as in the mid-segment near the EF-helix. This protection was expected, as these regions are either part of the ligand-binding site or involved in remote conformational changes where reduced HDX was observed. However, in both M-23- and tolcapone-bound states, residues spanning V29–E64 and D95–L111 exhibited greater cumulative

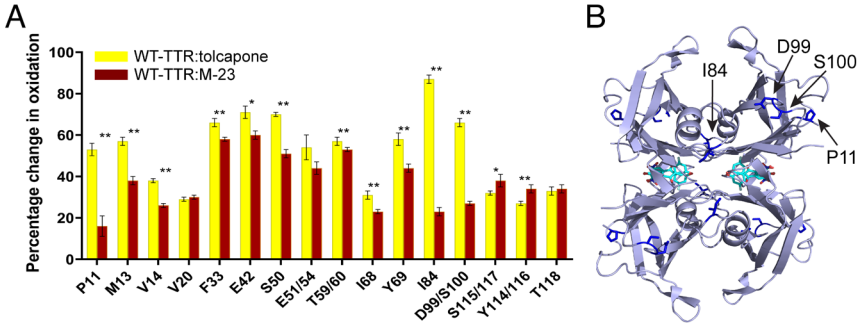

Fig. 3. FPOP analysis of the binding of M-23 and tolcapone to WT-TTR. (*A*) Changes in FPOP footprinting as a function of the ligands as determined by subtracting the residue-level oxidation of unbound from bound TTR. The tolcapone and M-23 bound state are represented by yellow and dark brown bars, respectively. The residues with the asterisk present significant statistical differences between tolcapone and M-23 bound states (*$P \le 0.05$; **$P \le 0.01$). The experiments were performed in triplicate. (*B*) Representation of the WT-TTR:M-23 crystal structure (PDB: 7QC5) with the side chain of residues P11, I84, and D99/S100 shown as blue sticks. These residues are labeled in one of TTR subunits to highlight their position.

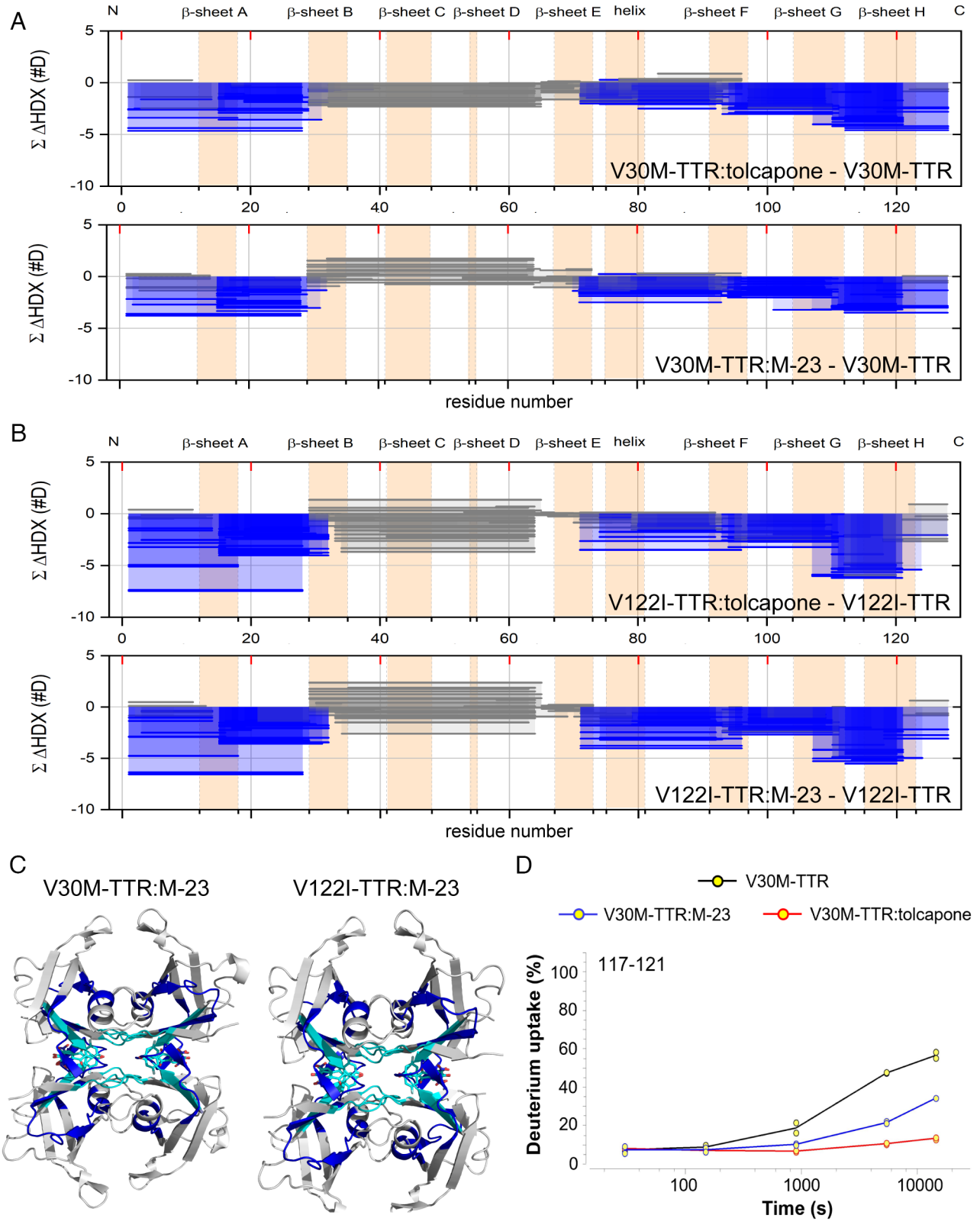

Fig. 4. Effect of M-23 and tolcapone on V30M- and V122I-TTR structure as examined by HDX-MS. (*A* and *B*) Woods' plots showing cumulative HDX differences on the Y-axis between the bound and unbound state for V30M-TTR (*A*) and V122I-TTR (*B*). Secondary structural elements of TTR are designated on top (peach shading). Peptides with statistically significant protection are shown in blue, whereas those from unaffected areas are in gray. (*C*) Statistically significant changes in HDX are mapped onto the crystal structure of the V30M-TTR:M-23 and V122I-TTR:M-23 complex. The regions closer to the binding pocket are colored in cyan, whereas those that are more remote (i.e., 19 to 28, 70 to 78 and 95 to 108) are shown in dark blue. TTR-tolcapone structures are not shown as the regions with decreased HDX are the same as for M-23. (*D*) HDX kinetics of V30M-TTR unbound (black) and bound to M-23 (blue) or tolcapone (red) for a peptide in the C-terminal region (117 to 121).

deuterium uptake in the V30M-bound state compared to the WT-Apo, suggesting that these regions remain more destabilized even upon ligand binding (*SI Appendix*, Tables S7 and S8). This is consistent with our previous observation, which showed a greater impact of the V30M mutation on the conformational dynamics of the protein, compared to V122I (Fig. 1 *A* and *B*).

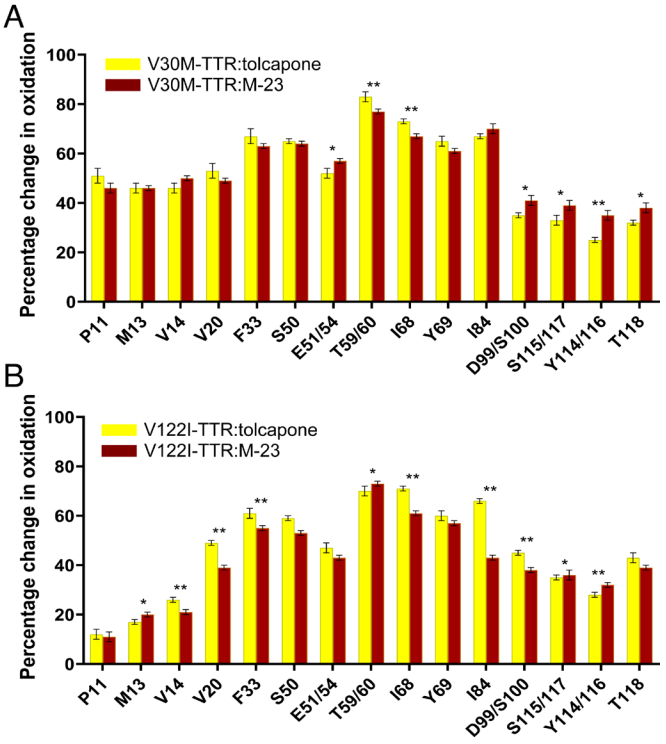

Fig. 5. FPOP analysis of the binding of M-23 and tolcapone to V30M-TTR (*A*) and V122I-TTR (*B*). The percentage change is determined by subtracting the residue-level footprinting of unbound from bound TTR. The tolcapone and M-23 bound state are represented by yellow and dark brown bars, respectively. The residues with the asterisk show significant statistical differences between tolcapone and M-23 bound states (*$P \leq 0.05$; **$P \leq 0.01$). The experiments were conducted in triplicate.

FPOP. FPOP footprinting analysis revealed that 15 residues in V30M- and V122I-TTR were significantly less oxidized after binding to M-23 and tolcapone (Fig. 5). As for WT-TTR, these residues include both residues that are inside or close to the binding site (M13, V14, V20, S50, E54, I84, Y114/116, S115/117, T118) and residues that are far from the binding site (P11, F33, E51, T59/60, I68, Y69, D99/S100), indicating both short and long-range stabilizing effects. Whereas the majority of residues from V30M-TTR exhibit a comparable effect with both compounds, residues E51/54, D99/S100, S115/117, Y114/116, and T118 exhibit a small but significant increase in oxidative footprinting, whereas residues T59/60 and I68 undergo a decrease in oxidative modification for the M-23-bound state compared to the tolcapone-bound state of V30M (Fig. 5). For V30M-TTR, the greatest protection upon binding was observed at the C-terminus, with tolcapone performing slightly better than M-23 for residues in this region, particularly those close to the binding site (Y114/116, S115/117, and T118) (Fig. 5*A* and *SI Appendix*, Table S4).

In the case of V122I-TTR, residues V14, V20, F33, I68, I84, and D99/S100 exhibit a decrease in footprinting, whereas residues M13, T59/60, and Y114/116 demonstrate an increase in footprinting for the M-23-bound state compared to the tolcapone-bound state of V122I mutant protein (Fig. 5*B* and *SI Appendix*, Table S4). As a general trend, for V122I-TTR, M-23 binding affords a better protected structure than does tolcapone based on oxidative footprinting. Both compounds show the most pronounced impact at the N-terminal region and a somewhat weaker effect at the C-terminus (Fig. 5*B*). As for WT-TTR, in V122I, the maximum protection differences between compounds occur at residue I84, near the binding channel's edge.

X-Ray Cocrystal Structures Fail to Predict the Conformational Impact of Kinetic Stabilizers. We analyzed the cocrystal structures of M-23 and tolcapone in complex with the pathogenic TTR variants. The crystal structures of V30M-TTR and V122I-TTR bound to M-23 were determined at 1.67 Å and 1.70 Å resolution, respectively (Fig. 6 *A* and *B* and *SI Appendix*, Table S9). We previously reported the cocrystal structure of tolcapone in complex with V30M-TTR (42) (1.57 Å) and V122I-TTR (34) (1.86 Å). As for the WT protein (33, 34), M-23 and tolcapone bind to V30M- and V122I-TTR in the so-called forward mode, with the 3,4-dihydroxy-5-nitrophenyl ring occupying the hydrophobic

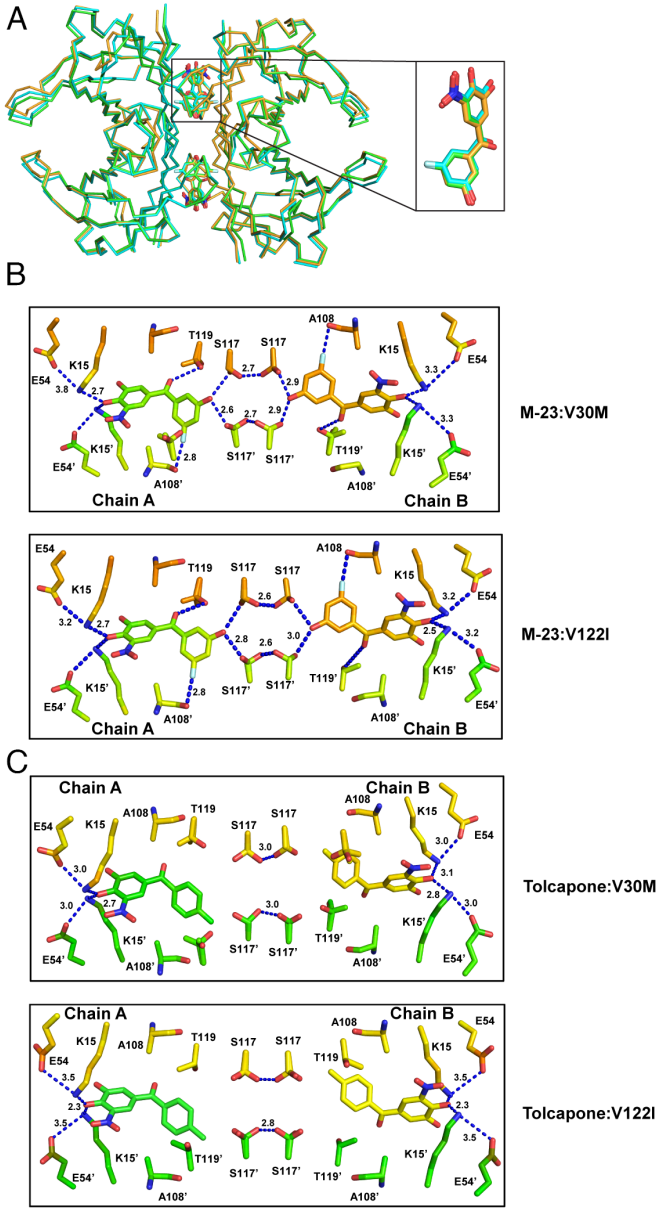

Fig. 6. Analysis of the X-ray crystal structures. (*A*) Superposition of WT-TTR (orange), V30M-TTR (green), and V122I-TTR (cyan) complexed to M-23. Overlaid tetramers are shown in ribbon, and M-23 is represented as sticks. The structural data for WT-TTR:M-23 were obtained from PDB file 7QC5. (*B*) M-23 binding at the TTR dimer–dimer interface for V30M (*Top*) and V122I (*Bottom*). M-23 and some of the TTR residues interacting with the ligand are represented by sticks. Dashed lines represent key interactions between M-23 and TTR and between the hydroxyl groups of S117/S117′. (*C*) Tolcapone binding at the V30M-TTR (*Up*) and V122I-TTR (*Bottom*) dimer–dimer interface. Ligand and some of the TTR residues interacting with the ligand are depicted by sticks. Dashed lines indicate relevant contacts between ligands and TTR and between the hydroxyl groups of S117/S117′.

Table 1. Thermodynamic parameters and stoichiometry (*n*) for the interaction of V30M- and V122I-TTR with M-23 and tolcapone analyzed by ITC

	M-23					Tolcapone				
	K_d(nM)	ΔG (kcal/mol)	ΔH (kcal/mol)	$-T\Delta S$ (kcal/mol)	*n*	K_d(nM)	ΔG (kcal/mol)	ΔH (kcal/mol)	$-T\Delta S$ (kcal/mol)	*n*
WT-TTR (33)	6.2	−11.2	−16.6	5.4	1.9	34	-10.2	−12.8	2.6	2.1
V30M-TTR	64	−9.8	−10.9	1.1	1.6	440	−8.7	−13.8	5.1	1.4
V122I-TTR	28	−10.3	−13.6	3.3	2.0	50	−10.0	−12.2	2.2	1.8

Error in ΔG is 0.1 kcal/mol and in ΔH and $-T\Delta S$ is 0.4 kcal/mol.

environment of the two symmetrical halogen-binding pockets, 2/2' and 1/1', which are located in the outer binding cavity (Fig. 6). The majority of TTR ligands, including T_4 (43), tafamidis (40), and acoramidis (44) adopt this binding mode. In this orientation, the 4-hydroxy substituent of M-23 and tolcapone can engage in hydrogen bonds with the ε-amino groups of K15/K15' residues of TTR, which in turn form salt bridges with the carboxylate group of E54/E54' (Fig. 6 *B* and *C*). These interactions were proposed to play a key role in stabilizing the protein–ligand interactions by restricting the entrance of solvent into the pocket (34). In both mutants, the central carbonyl group of M-23 establishes a hydrogen bond with the hydroxyl side chain of T119. In addition, the 3-F and 5-OH substituents of the 3-fluoro-5-hydroxyphenyl ring establish hydrogen bonds with carbonyl oxygen of A108 and the hydroxyl oxygen of S117/S117', respectively (Fig. 6*B*). These interactions in the inner binding cavity are not seen in the crystal structures of V30M- and V122I-TTR bound to tolcapone (Fig. 6*C*).

No evident long-range effects can be inferred for the two molecules in the crystal structures because, aside from the side chains in the binding site, the rest of the structure of the complexes is virtually identical to those of the corresponding unbound forms (45, 46). More importantly, the structures of M-23 and tolcapone in complex with V30M-TTR and V122I-TTR illustrate how the number of contacts in the crystal between the stabilizer and the TTR-tetramer is not a good proxy for the stabilizing effect the molecule exerts on the specific TTR variant in solution. The contacts that each kinetic stabilizer establishes with WT-TTR, V30M-TTR, and V122I-TTR in the respective cocrystals are identical, with the same interactions occurring with K15/K15', but a much higher number of contacts of M-23 in the inner binding cavity for all proteins. Despite this, according to HDX-MS and FPOP-MS, M-23 has a higher stabilizing effect on WT-TTR, whereas tolcapone is slightly more potent for V30M-TTR, especially at the protein C-terminus. These discrepancies likely reflect the failure of crystal structures to capture solvation effects and/or interaction strengths.

Binding Enthalpy Reflects Conformational Stability in TTR-Stabilizer Interactions. We evaluated the protective effect of the two stabilizers on V30M- and V122I-TTR by monitoring their unfolding kinetics in the presence of 6 M urea (*SI Appendix*, Fig. S11 *A* and *B*). Both compounds exhibit a strong stabilizing effect, with no apparent differences between them under the assay conditions. We then assessed their ability to prevent acid-induced aggregation at pH 4.4 (*SI Appendix*, Fig. S11 *C* and *D*). In this assay, both tolcapone and M-23 again showed potent inhibitory activity, although small differences were detected between the two molecules. These minor variations correlate with the trends observed by HDX-MS and FPOP for the corresponding TTR–ligand complexes. These results confirm the high efficacy of both stabilizers while illustrating the inherent limitations of these two gold-standard techniques in resolving subtle differences in conformational stability.

Next, we characterized the thermodynamics of V30M- and V122I-TTR interactions with M-23 and tolcapone by using isothermal titration calorimetry (ITC). As we previously reported for WT-TTR (33), both compounds bind to V30M-TTR and V122I-TTR without displaying negative cooperativity, in contrast to other stabilizers, like tafamidis (40) (Table 1 and *SI Appendix*, Fig. S12). Tolcapone and M-23 bind with higher affinity to V122I-TTR (K_d = 50 and 28 nM) than to V30M-TTR (K_d = 440 and 64 nM). This contrasts with the information from cocrystal structures that indicates that the interactions established by M-23 in the outer and inner binding cavity of V122I-TTR resemble those in V30M-TTR (Fig. 6 *A* and *B*).

In both TTR mutants, M-23 consistently showed a lower K_d than tolcapone, consistent with our previous findings for WT-TTR (Table 1) (33). This indicates that the binding affinity, as reflected in the binding free energy (ΔG), does not fully account for the differential conformational effects induced by the stabilizers, as revealed by HDX-MS and FPOP-MS. Investigators of recent studies (41) proposed that enthalpic contributions (ΔH), rather than affinity alone, more accurately reflect the kinetic stabilization potency of TTR ligands. In support of this view, the relative ΔH values measured for M-23 and tolcapone for the WT closely mirror the patterns observed in MS-based conformational analysis. Specifically, for WT-TTR and V122I-TTR $\Delta H_{M\text{-}23} > \Delta H_{tolcapone}$, whereas for V30M-TTR $\Delta H_{tolcapone} > \Delta H_{M\text{-}23}$. These results suggest that the strength of the TTR-stabilizer interactions, rather than overall binding free energy, better correlates with the extent of local and long-range conformational changes induced by the ligands.

Discussion

In this study, we employed MS-based structural footprinting—HDX-MS and FPOP—to investigate how pathogenic mutations and kinetic stabilizers impact the structure and dynamics of TTR in a near-native solution environment. Our findings not only bring insights to TTR but also underscore the limitations of conventional X-ray crystallography in capturing the dynamic conformational changes that underlie TTR destabilization and amyloid formation. In contrast, the MS-based approaches, which require only picomole amounts of protein, uncover mutation-specific and ligand-induced alterations in structural flexibility, more accurately reflecting the molecular basis of TTR pathology and therapeutic stabilization.

Our HDX-MS data provide compelling evidence that the V30M and V122I mutations destabilize TTR through distinct mechanisms. V30M, which resides in the hydrophobic core of β-strand B, induces widespread conformational perturbations extending to the FG loop and both β-sheets, consistent with a thermodynamic destabilization of the monomer. In contrast,

V122I, located at the dimer–dimer interface, causes localized increases in deuterium exchange, primarily affecting intersubunit contacts, such as β-strands F and G and the EF-helix, consistent with a kinetically destabilized tetramer. These distinct dynamic footprints are consistent with the destabilization mechanisms described for these variants in previous thermodynamic studies (6, 7), highlighting the need to understand the conformational context of individual TTR variants prior to designing therapeutic interventions.

Despite the nearly identical cocrystal structures of TTR bound to M-23 and tolcapone, HDX-MS and FPOP-MS uncover distinct local and long-range conformational changes induced by these ligands in WT-, V30M-, and V122I-TTR. M-23 consistently imparts greater stabilization to WT- and V122I-TTR, notably enhancing protection in the EF-helix and remote regions such as the FG loop. In contrast, tolcapone confers increased protection in the C-terminal region of V30M-TTR, suggesting enhanced efficacy for this specific variant. Although crystallography offers invaluable static snapshots, the sensitivity of HDX and FPOP to dynamics provides a deeper and more functional picture of how kinetic stabilizers influence the TTR conformational landscape.

FPOP-MS extends the conformational analysis to the residue level and confirms that kinetic stabilizers impact both proximal and distal residues from the binding pocket. M-23 in particular induces footprinting protection for distant residues such as D99/S100 and P11, suggesting a robust long-range stabilizing effect. These insights are essential for understanding the full extent of molecular stabilization and provide key information for designing compounds that exploit allosteric networks.

Our thermodynamic analysis further supports the notion that binding enthalpy (ΔH), not affinity (K_d or ΔG), better predicts the conformational stabilization imparted by kinetic stabilizers. The enthalpic profiles of M-23 and tolcapone correlate well with the magnitude and distribution of conformational protection observed in the HDX and FPOP data. For WT- and V122I-TTR, M-23 induces more favorable enthalpic interactions, whereas tolcapone is enthalpically more favorable for V30M-TTR. These results underscore the need to prioritize enthalpy-driven interactions during stabilizer design, particularly when aiming to enhance long-range conformational stability.

A recent cryo-EM study investigated the conformational landscape of TTR in the presence and absence of tafamidis (47). The study revealed intrinsic asymmetries within the tetramer and previously unobserved conformational states, providing mechanistic insight into the negatively cooperative ligand binding of this molecule. In our study, HDX-MS did not detect bimodal distributions in the peptide mass spectra, either in the absence or presence of stabilizers. Moreover, unlike tafamidis, tolcapone and M-23 bind to both T_4-binding sites with comparable affinities, showing no evidence of negative cooperativity. Although methodological differences cannot be entirely ruled out, our results suggest that the metastable conformational states identified by cryo-EM are not significantly populated under our experimental conditions.

Despite the well-established clinical efficacy of the kinetic stabilizers tafamidis, acoramidis, and diflunisal, these compounds present certain limitations related to potency, bioavailability, side effects, and limited blood–brain barrier permeability. Tolcapone and its derivative M-23 achieve strong enthalpy-driven stabilization and induce distinct conformational protection patterns in WT-, V30M-, and V122I-TTR. Their long-range stabilizing effects, broad variant coverage, together with their ability to cross the BBB suggest that these could expand the therapeutic landscape of TTR amyloidosis, particularly for variant-specific or neurological manifestations, and be used in novel combination therapies with TTR silencers (48).

One outcome of our research is that our findings reinforce the need for dynamic, solution-based characterization of protein–ligand interactions in the drug discovery pipeline for TTR amyloidosis and perhaps in other related systems. MS-based techniques offer critical insights not available through crystallography alone and allow for variant-specific evaluation of stabilizer efficacy. The ability to link conformational dynamics to thermodynamic signatures opens opportunities to design rationally specific stabilizers that optimize enthalpic contributions and target mutants' long-range structural vulnerabilities.

Future research should focus on expanding the application of HDX-MS and FPOP-MS to other amyloidogenic proteins and evaluating how these techniques can guide the development of therapeutics that target protein misfolding. Additionally, further correlation between enthalpy, long-range protection, and clinical efficacy in TTR and other protein systems might provide a robust framework for precision stabilization in conformational diseases.

Materials and Methods

TTR in vitro aggregation assays and tetramer stabilization assays are explained in the Supporting Information.

TTR Expression and Purification. The vectors encoding for V30M- and V122I-TTR were prepared by PCR site-directed mutagenesis using a pet28a vector (Novagen, Addgene, Cambridge, MA) encoding for the WT protein as a template. WT-TTR and TTR variants were recombinantly expressed and purified as explained before (35). The fractions eluting from the gel filtration chromatography were analyzed by SDS-PAGE and the ones with higher purity were combined and stored at −20 °C. Protein concentration was determined spectrophotometrically at 280 nm using a molar extinction coefficient of 77 600 M^{-1} cm^{-1}.

Synthesis Procedure. M-23 was prepared as previously reported (33). Tolcapone was purchased from Thermo Fisher Scientific (Waltham, MA).

HDX-MS Experiments. HDX-MS was performed to investigate nine TTR states, including WT, V122I, and V30M variants, both unbound and in complex with tolcapone or M-23. Comparative HDX-MS analysis enabled assessment of conformational dynamics and ligand-induced stabilization. HDX was initiated under controlled conditions and followed by online digestion, peptide separation, and mass spectrometric analysis. All HDX experiments were performed in duplicate to ensure reproducibility. Full experimental details, including sample preparation, LC–MS setup, peptide mapping, and data analysis, are provided in the Supporting Information.

FPOP-MS Experiments. FPOP-MS was used to assess solvent accessibility and structural changes in TTR variants, both unbound and bound to tolcapone or M-23. Hydroxyl radicals, generated by laser-induced Hâ„Oâ„ photolysis, reacted with TTR tetramers in the presence or absence of stabilizers. Oxidation was quenched immediately postirradiation, and samples were digested with trypsin prior to LC–MS/MS analysis. Modified and unmodified peptides were quantified to assess site-specific oxidation. All experiments were performed in triplicate, including nonirradiated controls to account for background oxidation. Detailed protocols for FPOP labeling, LC–MS/MS setup, data analysis, and quantification of oxidation levels are provided in the Supporting Information.

Isothermal Titration Calorimetry. The binding parameters for both ligands, tolcapone and M-23, interacting with V122I-TTR and V30M-TTR were measured by ITC, the gold standard for the thermodynamic study of biomolecular interactions (49). All ITC measurements were performed with protein and compounds dissolved in the same buffer (PBS buffer pH 7.0, containing 100 mM KCl, 1mM EDTA, and 2.5% DMSO), and degassed. The ITC measurements were performed at 25 °C using a Nano ITC calorimeter (TA Instruments, New Castle, DE). Titrations were carried out as a set of 20 injections of 100 μM compound into protein (5 μM), programmed as 2.02 μl injections with 150 s of equilibration time spacing.

Peak integration was done using the NanoAnalyze software (TA Instruments) and the data analyzed using a general model for a protein with two ligand-binding sites implemented in Origin 7.0 (OriginLab, Northampton, MA), which accounts for the potential existence of cooperative binding within the homodimeric protein (50, 51).

Crystallization and Structure Determination. Cocrystals of V30M-TTR/M-23, V122I-TTR/M-23, and V30M-TTR/tolcapone were obtained as previously reported (35). In short, purified proteins (140 μM) were mixed with 10-fold molar excess of M-23/tolcapone and cocrystallized at 18 °C by hanging-drop vapor diffusion by mixing equal amounts of complex and reservoir solution. The reservoir solution contained 25 to 30% PEG 400, 200 mM $CaCl_2$, 100 mM HEPES, pH 7.0 to 7.5. The crystals were flash-frozen in liquid nitrogen (100 K), and diffraction data were recorded at the BL13-XALOC beamline from the ALBA Synchrotron in Barcelona (52). Data were integrated and merged using XDS (53) and scaled, reduced, and further analyzed with CCP4 (54). The structures of TTR/M-23 and V30M-TTR/tolcapone complexes were determined by molecular replacement with Phenix (version 1.19.2-4158) (55) using a previous TTR structure (PDB 1F41) as a search model. Model refinement was done using Phenix (55), and model building was performed with Coot (56). Figures were prepared using Pymol (The PyMOL Molecular Graphics System, Version 2.0, Schrödinger, LLC, Palo Alto, CA).

Data, Materials, and Software Availability. Atomic coordinates and the structure factors data have been deposited in the RCSB Protein Data Bank under the accession codes 9H5Y (V30M-TTR:M-23) (57) and 9H5X (V122I-TTR:M-23) (58). HDX-MS and FPOP-MS data have been deposited to the ProteomeXchange Consortium via the PRIDE (59) partner repository with the dataset identifiers PXD071902 (60) and PXD071928 (61), respectively. All other data are included in the article and/or *SI Appendix*.

ACKNOWLEDGMENTS. This work was funded by the Spanish Ministry of Science and Innovation (PID2022-137963OB-I00), by ICREA (ICREA-Academia 2020), and by the Agency for Management of University and Research Grants (AGAUR) (2021 SGR 00635) to S.V. and M.L.G. acknowledges the financial support from the National Institute of Health (NIH) (R24GM136766 and R01AG079283). A.V.-C. acknowledges the Spanish Ministry of Science and Innovation (MCIN/AEI/10.13039/501100011033/) and "ERDF A way of Making Europe" (PID2021-127296OB-I00). This work was supported by the Spanish Ministry of Science and Innovation (PID2021-124602OB-I00) and by the Agency for Management of University and Research Grants (AGAUR) (2021 SGR 00635) to D.V. Portions of the paper were developed from the thesis of F.P.

Author affiliations: [a]Institut de Biotecnologia i Biomedicina and Departament de Bioquímica i Biologia Molecular, Universitat Autònoma de Barcelona, Barcelona 08193, Spain; [b]Department of Chemistry, Washington University, St. Louis, MO 63130; [c]Faculty of Sciences, Department of Biochemistry and Molecular and Cellular Biology, Institute of Biocomputation and Physics of Complex Systems, Universidad de Zaragoza, Zaragoza 50018, Spain; [d]Institute for Health Research Aragon (Instituto de Investigación Sanitaria Aragón), Zaragoza 50009, Spain; [e]Networking Biomedical Research Centre in Liver and Digestive Diseases, Madrid 28029, Spain; [f]Department of Biochemistry and Molecular and Cell Biology, University of Zaragoza, Zaragoza 50009, Spain; and [g]Institut d'Investigació i Innovació Parc Taulí - Catalan Network of Research Centers, Sabadell 08208, Spain

Author contributions: F.P., R.K., S.C., I.P., M.L.G., and S.V. designed research; F.P., R.K., S.C., N.V., and A.V.-C. performed research; F.P., R.K., N.V., A.V.-C., D.R., I.P., M.L.G., and S.V. analyzed data; and F.P., R.K., I.P., M.L.G., and S.V. wrote the paper.

The authors declare no competing interest.

1. M. D. Benson, Transthyretin amyloidosis: A little history of hereditary amyloidosis. *Amyloid* **24**, 76–77 (2017).
2. C. C. Blake, M. J. Geisow, S. J. Oatley, B. Rérat, C. Rérat, Structure of prealbumin: Secondary, tertiary and quaternary interactions determined by Fourier refinement at 1.8 A. *J. Mol. Biol.* **121**, 339–356 (1978).
3. C. C. Blake, M. J. Geisow, I. D. Swan, C. Rerat, B. Rerat, Structure of human plasma prealbumin at 2–5 A resolution. A preliminary report on the polypeptide chain conformation, quaternary structure and thyroxine binding. *J. Mol. Biol.* **88**, 1–12 (1974).
4. T. R. Foss, R. L. Wiseman, J. W. Kelly, The pathway by which the tetrameric protein transthyretin dissociates. *Biochemistry* **44**, 15525–15533 (2005).
5. Z. Lai, W. Colón, J. W. Kelly, The acid-mediated denaturation pathway of transthyretin yields a conformational intermediate that can self-assemble into amyloid. *Biochemistry* **35**, 6470–6482 (1996).
6. A. R. Hurshman Babbes, E. T. Powers, J. W. Kelly, Quantification of the thermodynamically linked quaternary and tertiary structural stabilities of transthyretin and its disease-associated variants: The relationship between stability and amyloidosis. *Biochemistry* **47**, 6969–6984 (2008).
7. P. Hammarström, X. Jiang, A. R. Hurshman, E. T. Powers, J. W. Kelly, Sequence-dependent denaturation energetics: A major determinant in amyloid disease diversity. *Proc. Natl. Acad. Sci. U.S.A.* **99**, 16427–16432 (2002).
8. D. R. Jacobson *et al.*, Variant-sequence transthyretin (isoleucine 122) in late-onset cardiac amyloidosis in black Americans. *N. Engl. J. Med.* **336**, 466–473 (1997).
9. C. Andrade, A peculiar form of peripheral neuropathy; Familiar atypical generalized amyloidosis with special involvement of the peripheral nerves. *Brain* **75**, 408–427 (1952).
10. M. J. Saraiva, S. Birken, P. P. Costa, D. S. Goodman, Amyloid fibril protein in familial amyloidotic polyneuropathy, Portuguese type. Definition of molecular abnormality in transthyretin (prealbumin). *J. Clin. Invest.* **74**, 104–119 (1984).
11. H. Goren, M. C. Steinberg, G. H. Farboody, Familial oculoleptomeningeal amyloidosis. *Brain* **103**, 473–495 (1980).
12. Y. Sekijima *et al.*, Energetic characteristics of the new transthyretin variant A25T may explain its atypical central nervous system pathology. *Lab. Invest.* **83**, 409–417 (2003).
13. P. Westermark, K. Sletten, B. Johansson, G. G. Cornwell, Fibril in senile systemic amyloidosis is derived from normal transthyretin. *Proc. Natl. Acad. Sci. U.S.A.* **87**, 2843–2845 (1990).
14. A. Hörnberg, T. Eneqvist, A. Olofsson, E. Lundgren, A. E. Sauer-Eriksson, A comparative analysis of 23 structures of the amyloidogenic protein transthyretin. *J. Mol. Biol.* **302**, 649–669 (2000).
15. S. M. Johnson *et al.*, Native state kinetic stabilization as a strategy to ameliorate protein misfolding diseases: A focus on the transthyretin amyloidoses. *Acc. Chem. Res.* **38**, 911–921 (2005).
16. Y. Sekijima, K. Tojo, H. Morita, J. Koyama, S. Ikeda, Safety and efficacy of long-term diflunisal administration in hereditary transthyretin (ATTR) amyloidosis. *Amyloid* **22**, 79–83 (2015).
17. F. A. Barroso *et al.*, Long-term safety and efficacy of tafamidis for the treatment of hereditary transthyretin amyloid polyneuropathy: Results up to 6 years. *Amyloid* **24**, 194–204 (2017).
18. M. S. Maurer *et al.*, Tafamidis treatment for patients with transthyretin amyloid cardiomyopathy. *N. Engl. J. Med.* **379**, 1007–1016 (2018).
19. J. D. Gillmore *et al.*, Efficacy and safety of acoramidis in transthyretin amyloid cardiomyopathy. *N. Engl. J. Med.* **390**, 132–142 (2024).
20. C. Monteiro *et al.*, Predictive model of response to tafamidis in hereditary ATTR polyneuropathy. *JCI Insight* **4**, e126526 (2019).
21. F. Salvi *et al.*, Failure of Tafamidis to halt progression of Ala36Pro TTR oculomeningovascular amyloidosis. *J. Stroke Cerebrovasc. Dis.* **27**, e212–e214 (2018).
22. C. Monteiro *et al.*, Cerebrospinal fluid and vitreous body exposure to orally administered tafamidis in hereditary ATTRV30M (p.TTRV50M) amyloidosis patients. *Amyloid* **25**, 120–128 (2018).
23. S. K. Palaninathan, Nearly 200 X-ray crystal structures of transthyretin: What do they tell us about this protein and the design of drugs for TTR amyloidoses?. *Curr. Med. Chem.* **19**, 2324–2342 (2012).
24. M. Cheng, M. L. Gross, Mass spectrometry-based protein footprinting for protein structure characterization. *Acc. Chem. Res.* **58**, 165–176 (2025).
25. K. S. Li, L. Shi, M. L. Gross, Mass spectrometry-based fast photochemical oxidation of proteins (FPOP) for higher order structure characterization. *Acc. Chem. Res.* **51**, 736–744 (2018).
26. E. I. James, T. A. Murphree, C. Vorauer, J. R. Engen, M. Guttman, Advances in hydrogen/deuterium exchange mass spectrometry and the pursuit of challenging biological systems. *Chem. Rev.* **122**, 7562–7623 (2022).
27. S. Kailasan *et al.*, Antigenic landscapes on *Staphylococcus aureus* pore-forming toxins reveal insights into specificity and cross-neutralization. *MAbs* **14**, 2083467 (2022).
28. R. Kant *et al.*, Small molecule assembly agonist alters the dynamics of hepatitis B virus core protein dimer and capsid. *J. Am. Chem. Soc.* **146**, 28856–28865 (2024).
29. D. M. Hambly, M. L. Gross, Laser flash photolysis of hydrogen peroxide to oxidize protein solvent-accessible residues on the microsecond timescale. *J. Am. Soc. Mass Spectrom.* **16**, 2057–2063 (2005).
30. K. S. Li *et al.*, Hydrogen–deuterium exchange and hydroxyl radical footprinting for mapping hydrophobic interactions of human bromodomain with a small molecule inhibitor. *J. Am. Soc. Mass Spectrom.* **30**, 2795–2804 (2019).
31. O. Cornwell, S. E. Radford, A. E. Ashcroft, J. R. Ault, Comparing hydrogen deuterium exchange and fast photochemical oxidation of proteins: A structural characterisation of wild-type and ΔN6 β2-microglobulin. *J. Am. Soc. Mass Spectrom.* **29**, 2413–2426 (2018).
32. Y. Zhang *et al.*, Pulsed hydrogen–deuterium exchange mass spectrometry probes conformational changes in amyloid beta (Aβ) peptide aggregation. *Proc. Natl. Acad. Sci. U.S.A.* **110**, 14604–14609 (2013).
33. F. Pinheiro *et al.*, Development of a highly potent transthyretin amyloidogenesis inhibitor: Design, synthesis, and evaluation. *J. Med. Chem.* **65**, 14673–14691 (2022).
34. R. Sant'Anna, *et al.*, Repositioning tolcapone as a potent inhibitor of transthyretin amyloidogenesis and associated cellular toxicity. *Nat. Commun.* **7**, 10787 (2016).
35. F. Pinheiro *et al.*, Tolcapone, a potent aggregation inhibitor for the treatment of familial leptomeningeal amyloidosis. *FEBS J.* **288**, 310–324 (2021).
36. C. Rapezzi *et al.*, Transthyretin-related amyloidoses and the heart: A clinical overview. *Nat. Rev. Cardiol.* **7**, 398–408 (2010).
37. X. Jiang, J. N. Buxbaum, J. W. Kelly, The V122I cardiomyopathy variant of transthyretin increases the velocity of rate-limiting tetramer dissociation, resulting in accelerated amyloidosis. *Proc. Natl. Acad. Sci. U.S.A.* **98**, 14943–14948 (2001).
38. S. K. Palaninathan, N. N. Mohamedmohaideen, W. C. Snee, J. W. Kelly, J. C. Sacchettini, Structural insight into pH-induced conformational changes within the native human transthyretin tetramer. *J. Mol. Biol.* **382**, 1157–1167 (2008).
39. J. A. Ferguson, X. Sun, H. J. Dyson, P. E. Wright, Thermodynamic stability and aggregation kinetics of EF helix and EF loop variants of transthyretin. *Biochemistry* **60**, 756–764 (2021).
40. C. E. Bulawa *et al.*, Tafamidis, a potent and selective transthyretin kinetic stabilizer that inhibits the amyloid cascade. *Proc. Natl. Acad. Sci. U.S.A.* **109**, 9629–9634 (2012).
41. M. Miller *et al.*, Enthalpy-driven stabilization of transthyretin by AG10 mimics a naturally occurring genetic variant that protects from transthyretin amyloidosis. *J. Med. Chem.* **61**, 7862–7876 (2018).
42. F. Pinheiro *et al.*, PITB: A high affinity transthyretin aggregation inhibitor with optimal pharmacokinetic properties. *Eur. J. Med. Chem.* **261**, 115837 (2023).

43. A. Wojtczak, V. Cody, J. R. Luft, W. Pangborn, Structures of human transthyretin complexed with thyroxine at 2.0 A resolution and 3′, 5′-dinitro-N-acetyl-L-thyronine at 2.2 A resolution. *Acta Crystallogr. D Biol. Crystallogr.* **52**, 758–765 (1996).
44. S. C. Penchala *et al.*, AG10 inhibits amyloidogenesis and cellular toxicity of the familial amyloid cardiomyopathy-associated V122I transthyretin. *Proc. Natl. Acad. Sci. U.S.A.* **110**, 9992–9997 (2013).
45. L. Saelices *et al.*, Uncovering the mechanism of aggregation of human transthyretin. *J. Biol. Chem.* **290**, 28932–28943 (2015).
46. A. M. Damas, S. Ribeiro, V. S. Lamzin, J. A. Palha, M. J. Saraiva, Structure of the Val122Ile variant transthyretin - A cardiomyopathic mutant. *Acta Crystallogr. D Biol. Crystallogr.* **52**, 966–972 (1996).
47. B. Basanta *et al.*, The conformational landscape of human transthyretin revealed by cryo-EM. bioRxiv [Preprint] (2024). https://doi.org/10.1101/2024.01.23.576879 (Accessed 23 January 2024).
48. T. N. Qarni *et al.*, Treatment characteristics of patients with hereditary transthyretin amyloidosis: A cohort study. *Orphanet J. Rare Dis.* **19**, 191 (2024).
49. M. Bastos *et al.*, Isothermal titration calorimetry. *Nat. Rev. Methods Primers* **3**, 17 (2023).
50. E. Freire, A. Schön, A. Velazquez-Campoy, Isothermal titration calorimetry: General formalism using binding polynomials. *Methods Enzymol.* **455**, 127–155 (2009).
51. S. Vega, O. Abian, A. Velazquez-Campoy, A unified framework based on the binding polynomial for characterizing biological systems by isothermal titration calorimetry. *Methods* **76**, 99–115 (2015).
52. J. Juanhuix *et al.*, Developments in optics and performance at BL13-XALOC, the macromolecular crystallography beamline at the ALBA synchrotron. *J. Synchrotron Radiat.* **21**, 679–689 (2014).
53. W. Kabsch, Integration, scaling, space-group assignment and post-refinement. *Acta Crystallogr. D Biol. Crystallogr.* **66**, 133–144 (2010).
54. M. D. Winn *et al.*, Overview of the CCP4 suite and current developments. *Acta Crystallogr. D Biol. Crystallogr.* **67**, 235–242 (2011).
55. P. D. Adams *et al.*, PHENIX: A comprehensive Python-based system for macromolecular structure solution. *Acta Crystallogr. D, Biol. Crystallogr.* **66**, 213–221 (2010).
56. P. Emsley, B. Lohkamp, W. G. Scott, K. Cowtan, Features and development of coot. *Acta Crystallogr. D Biol. Crystallogr.* **66**, 486–501 (2010).
57. N. Varejao, F. Pinheiro, I. Pallares, S. Ventura, D. Reverter, Data from "Crystal structure of human V30M transthyretin in complex with (3,4-dihydroxy-5-nitrophenyl)-(3-fluoro-5-hydroxyphenyl) methanone compound." RCSB Protein Data Bank. https://www.rcsb.org/structure/9H5Y. Deposited 23 October 2024.
58. N. Varejao, F. Pinheiro, I. Pallares, S. Ventura, D. Reverter, Data from "Crystal structure of human V122I transthyretin in complex with (3,4-dihydroxy-5-nitrophenyl)-(3-fluoro-5-hydroxyphenyl) methanone compound." RCSB Protein Data Bank. https://www.rcsb.org/structure/9H5X. Deposited 23 October 2024.
59. P. Jones *et al.*, PRIDE: A public repository of protein and peptide identifications for the proteomics community. *Nucleic Acids Res.* **34**, D659–D663 (2005).
60. R. Kant, M. Gross, Mass spectrometry footprinting reveals how kinetic stabilizers counteract transthyretin dynamics altered by pathogenic mutations. PRIDE. https://www.ebi.ac.uk/pride/archive/projects/PXD071902. Deposited 12 December 2025.
61. R. Kant, M. Gross, Mass spectrometry footprinting reveals how kinetic stabilizers counteract transthyretin dynamics altered by pathogenic mutations_FPOP. PRIDE. https://www.ebi.ac.uk/pride/archive/projects/PXD071928. Deposited 12 December 2025.